Comparative Evaluation of Threshold Pressure Measurement Techniques in Faulted and Shale Formations

Authors and affiliations:

Akpewe M. Eroh: a.m.eroh@leeds.ac.uk University of Leeds, School of Earth and Environment

Paul W.J. Glover: P.W.J.Glover@leeds.ac.uk University of Leeds, School of Earth and Environment

Samuel Allshorn: S.Allshorn@leeds.ac.uk University of Leeds, School of Earth and Environment

This is a non-peer reviewed preprint submitted to EarthArXiv.

Abstract. Reliable estimation of capillary threshold pressure is essential for evaluating the sealing capacity of subsurface flow barriers, which has important applications in fluid storage. This study compares the results of capillary threshold pressure measurements obtained from four experimental techniques: (i) gas breakthrough, (ii) mercury injection capillary pressure (MICP), (iii) Porosimetry under Confining Stress (PUCS), and (iv) Field's metal injection with SEM imaging, applied to faulted sandstone from the Vale of Eden and mudstone from the Sidmouth Formation of the Mercia Mudstone Group (MMG). Gas breakthrough tests demonstrated strong internal consistency and repeatability; however, the technique is inherently slow and has very low throughput, often requiring several months to complete a single test on a typical mudstone sample. The MICP method exhibited considerable variability among the analysed samples and was unable to access the matrix porosity of mudstone due to compressibility and pore structure collapse. Mercury instead, preferentially occupied fractures and micro-cracks, as confirmed by SEM imaging of Field's metal injection, an artefact that is often misinterpreted as mercury filling pore volume. Field's metal injection yielded higher threshold pressures and provided valuable pore-scale insights from SEM imaging, but the method lacks standardized conversion parameters, making comparison with other methods difficult. These findings underscore the limitations of conventional methods in characterizing tight formations and highlight the need for caution when interpreting MICP results, particularly for shale and other low-permeability rocks. Furthermore, they emphasize the importance of developing a robust experimental framework that addresses these shortcomings, especially for tight gas and shale formations where accurate measurement of flow properties is critical for subsurface storage applications, including CO_2 sequestration and the disposal of nuclear waste in deep geological repositories.

Keywords. Capillary threshold pressure, Mercury Injection Capillary Pressure (MICP), Porosimeter under Confining Stress (PUCS), Field's metal Injection (FMI), Clay-rich-Shale, Scanning Electron Microscope (SEM), gas breakthrough.

INTRODUCTION

Global transition toward clean energy systems and the attainment of net-zero carbon emissions necessitate a multi-faceted technological framework, with carbon management playing a central role (Pokharel and Rijal, 2021; Wehbi, 2024). Geological storage of carbon dioxide (CO_2) and the deep subsurface disposal of nuclear waste represent two critical strategies for mitigating anthropogenic climate change and managing long-lived hazardous materials (Claret et al., 2018; Fisher et al., 2023). These approaches rely on the integrity of geological formations to ensure long-term containment, and their effectiveness is contingent upon a thorough understanding of subsurface processes, material behaviour, and risk assessment (Jenkins et al., 2024).

Shale formations, owing to their ultra-low permeability, are regarded as among the most effective natural subsurface barriers to fluid migration, particularly in the context of radioactive nuclear waste disposal in underground repositories and as caprock above CO_2 storage sites (Fisher et al., 2023). For effective CO_2 storage, however, a reservoir rock with high porosity and permeability is essential to facilitate efficient injection and migration of the gasp phase. Faulted sandstones are often considered suitable for this purpose, as they can serve both as reservoirs and as lateral seals that restrict CO_2 migration along fault planes (Pasala et al., 2013; Fisher et al., 2023; He et al., 2024).

Studies have shown that fault architecture significantly influences CO_2 storage and migration efficiency. For instance, Pasala et al. (2013) showed through numerical simulations that ultra-low fault zones characterised by deformation bands can enhance CO_2 containment through reservoir compartmentalisation, whereas high-permeability fault zones dominated by fracture networks may act as vertical conduit, reducing storage efficiency. He et al. (2024) examined the geomechanical stability of tight sandstone reservoirs under dynamic CO_2 injection, highlighting the potential for mineral dissolution and weakening of rock strength due to the interaction with carbonic acid (H_2CO_3).

A critical aspect of the transition to secure subsurface storage systems is the prevention of leakage over geological timescales (Le et al., 2009; Eke et al., 2021). Potential leakage pathways may arise from radionuclide mobility (Toulhoat, 2002), CO_2 buoyancy-driven pressure, and the induction or reactivation of fractures (Fisher et al., 2023) due to fluid injection. Ensuring long-term containment under such conditions requires a comprehensive assessment and characterisation of geological flow barriers, including the top seal (caprock) and fault seal capillary entry or threshold pressure, and seal capacity, which defines the maximum column height a seal can retain before leakage. Recent research has demonstrated that fluid injection

can drastically alter *in-situ* stress field, potentially causing fault reactivation and enhancement of permeability. Pulchan et al. (2020) reported that fault reactivation during combined CO_2-EOR and storage operation can either enhance storage capacity or initiate leakage, depending on fault properties and injection pressure. Lee et al. (2023) conducted coupled multiphase flow and geomechanical simulations to evaluate the probability of shear slip in fractured caprock during CO_2 injection, highlighting the importance of site-specific stress regimes.

A major challenge in subsurface containment is the accurate measurement and characterisation of the flow properties of geological storage barriers, particularly the threshold pressure in shale formations (Bust et al., 2013; Liu, H.H., 2014). Over the years, several experimental techniques have been employed to determine the capillary entry pressure of top seals and fault zones. Among these, the mercury injection capillary pressure (MICP) technique first used by Purcell (1949) to calculate permeability has gained widespread acceptance due to its unique capabilities and the relatively short duration required to conduct tests compared to methods such as dynamic gas displacement (Falode and Manuel, 2014). The MICP approach has proven effective for formations with moderate to high permeability and can be used to estimate permeability accurately in such formations (Rashid et al., 2015). However, its applicability to shale formations has been questioned, as the high surface tension and contact angle of mercury are believed to limit its ability to access the fine pore structures characteristic of shale (e.g., Hildenbrand and Urai, 2003; Klaver et al., 2015).

Furthermore, the MICP technique currently in use does not apply confining stress to shale samples, even though many petrophysical properties, such as capillary pressure and permeability, are known to be stress-sensitive (Guise et al., 2024). This limitation raises concerns about the reliability of MICP results for low-permeability formations like shale. Therefore, proactive approaches to validate the method are required to address concerns about the reliability of MICP in evaluating shale petrophysical properties.

This study presents a comparative analysis of experimental techniques used to estimate capillary threshold pressure of subsurface flow barriers. The primary objective is to evaluate the reliability and applicability of Mercury Injection Capillary Pressure (MICP) in characterising low-permeability formations, particularly shale, under realistic stress conditions. To achieve this, we employ a suite of methods including (i) MICP, (ii) Porosimeter under Confining Stress (PUCS), (iii) dynamic gas displacement, and (iv) Field's metal injection, together with Scanning Electron Microscopy (SEM). These techniques are applied to mudstones from the Mercia Mudstone Group (MMG), the Sidmouth Mudstone Formation, and faulted sandstones

from the Vale of Eden. Field's metal injection and SEM imaging are further used to validate MICP results by enabling direct visualisation of pore structures. By integrating findings across these methods, the study aims to identify their respective strengths and limitations and provide recommendations for their use in geological storage projects. The findings enhance understanding of subsurface barrier performance and inform the predictive models for leakage risk and long-term containment.

1. Fluid transport and capillary pressure in mudstone and faulted sandstone

Fluid transport at the pore scale in sedimentary rocks is controlled by both capillary and viscous forces (). Capillary forces dominate the initial displacement of a wetting fluid by a non-wetting phase in brine-saturated rocks, resisting invasion and influencing sealing capacity. Capillary pressure, P_c, defined as the pressure difference between the non-wetting, and wetting phases, arises from interfacial tension and curvature at the fluid interface:

$$P_c = P_{nw} - P_w \quad \textbf{(1)}$$

where P_{nw} and P_w are the pressures in the non-wetting and wetting phases, respectively. These pressures arise due to the imbalance of forces at the fluid interfaces, driven by intermolecular attractions within each phase and their interaction (wettability) with the solid surface. According to the Young–Laplace equation capillary pressure increases with interfacial tension and wettability and decreases with larger pore throat radius. These relationships explain why mudstones with nano-scale pores and water-wet conditions exhibit high threshold pressures:

$$P_c = \frac{-2\gamma\cos\theta}{r} \quad \textbf{(2)}$$

Two key capillary pressures govern gas invasion: entry pressure and breakthrough pressure. Entry pressure represents the minimum pressure required for the non-wetting phase to displace the wetting phase from the largest interconnected pores (Hildenbrand et al., 2004; 2016). This condition is expressed as:

$$P_{nw} > P_w + P_c. \quad \textbf{(3)}$$

As pore sizes decrease, the non-wetting phase must overcome progressively higher capillary barriers until a continuous pathway forms. The pressure at which this occurs is the breakthrough pressure, which provides critical insight into sealing capacity and is strongly influenced by interfacial tension, contact angle, and pore geometry (Purcell, 1950).

Once the capillary threshold is exceeded, viscous forces govern macroscopic fluid movement. Viscous forces represent resistance to flow due to internal friction and drag against pore walls. This process is described by Darcy's law:

$$q = -\frac{k}{\mu}\Delta P \quad \textbf{(4)}$$

where q is the Darcy flux express as the volumetric flow rate per unit area in m/s, k is the intrinsic permeability of the medium expressed in the units of m^2 or mD, μ is the dynamics fluid viscosity of the fluid in Pa.s, and ΔP is the pressure gradient in Pa/m. While permeability reflects the ease of flow through the rock, viscosity controls resistance to deformation (Chen et al., 2021; Bonazzi et al., 2021). Ultimately, fluid transport in sedimentary rocks is a balance between capillary forces, which control initial entry and distribution, and viscous forces, which dictate bulk flow once connectivity is established.

2.1 Mercury injection capillary pressure (MICP)

The principles governing capillary pressure and fluid transport at the pore scale form the basis for experimental techniques such as Mercury Injection Capillary Pressure (MICP). MICP applies the Young–Laplace relationship by using mercury, a strongly non-wetting fluid, to invade pore spaces under controlled pressure increments (Purcell, 1949; Siqveland & Skjæveland, 2021). This technique quantifies pore throat size distribution and determines key sealing parameters, including threshold and breakthrough pressures, which directly correspond to the theoretical concepts discussed above. By progressively increasing injection pressure, MICP reproduces the capillary barriers encountered during multiphase flow in brine-saturated rocks and enables prediction of sealing capacity in mudstones and faulted sandstones (Geng et al., 2024). In this way, MICP serves as a practical extension of capillary pressure theory, converting interfacial tension and pore geometry effects into measurable data for reservoir and caprock integrity assessment (Brown, 2015; Olson & Grigg, 2008).

Mercury Injection Capillary Pressure (MICP) testing was first introduced by Purcell (1949) as a method for estimating the permeability of porous formations. Since its development, MICP has become widely used due to its effectiveness and ease of application in characterising the physical properties of sedimentary basins, including pore size distribution (PSD), relative permeability, and capillary pressure, particularly for evaluating top seals and fault seals relevant to subsurface fluid storage. Olson and Grigg (2008) demonstrated that MICP can accurately estimate matrix porosity and permeability in tight formations such as shale. Jennings (1987) highlighted its application in assessing reservoir quality, fluid distribution, and seal capacity, including hydrocarbon column heights. Davudov et al. (2018) refined the method by introducing corrections for conformance, grain compressibility, and inaccessible pore compression, emphasising the importance of accounting for all compressibility effects to achieve accurate reservoir evaluation in shales.

Mercury, being a non-wetting fluid, does not enter pore spaces by capillary action because of its high surface tension and large contact angle (Webb and Orr, 1997). Instead, it must be forcibly intruded into the porous medium. According to Washburn (1921), the pressure required to inject mercury into a pore is inversely proportional to the pore diameter, as described by the Washburn equation:

$$P_c = \frac{-4\gamma\cos\theta}{D}, \quad \textbf{(5)}$$

where γ is the surface tension of mercury, D is the pore diameter, and θ is the contact angle. The equation suggests, for example, that assuming a surface tension of 0.485 N/m and a contact angle of 130° at ambient temperature, mercury can intrude into pores as small as 0.003 μm at a pressure of approximately 60,000 psia (413.69 MPa) (Webb and Orr, 1997). This relationship allows the pore throat sizes characterisation and determination of sealing capacity from pressure measurements during mercury intrusion. The use of standard Mercury Injection Capillary Pressure (MICP) to characterise rock properties has faced criticism. Standard MICP typically employs small rock samples, which may not accurately represent the heterogeneity of entire reservoirs (Comisky et al., 2011). Furthermore, the method does not apply confining stress during testing, even though formation properties are known to be stress-sensitive (Guise et al., 2018). These limitations raise concerns about the reliability of measurements, despite arguments that mercury exerts an isostatic pressure on the sample. In this study, both standard (unstressed) MICP and stressed MICP, also known as Porosimetry under Confining Stress (PUCS), are employed. The following section outlines the experimental procedures.

2. METHODS AND MATERIALS

2.1 Sample preparation

The material studied comprises faulted sandstone from the Vale of Eden in Cumbria, northwest England (**54.70001° N, −2.66667° W**), and Triassic mudstone from the Mercia Mudstone Group, specifically the Sidmouth Mudstone Formation, exposed in coastal cliffs near the River Sid on the south Devon coast, Weston Beach (**50.68515° N, −3.18413° W**). Material preparation was tailored to the requirements of each experimental method. Dynamic gas breakthrough, MICP, PUCS, and Field's metal injection were performed on full core plugs, while for MICP, samples of approximately 1 cm³ were used. Core trimming and plugging were carried out with a precision saw to isolate undisturbed sections. Both formations were plugged in the laboratory using a 38 mm diamond drill bit. The faulted sandstone was drilled using water as the drilling fluid, while air was used for the mudstone due to the presence of sensitive clay minerals that could react with water and alter the pore structure. Ewy (2015) noted that exposing shales to water when they are not under stress can damage their microstructure, potentially invalidating subsequent laboratory testing. The samples obtained has dimensions that vary between 2.00 cm to 5.60 cm in length, and 3.73 cm to 3.79 cm in diameter. Samples were weighed and cleaned using Soxhlet extraction with toluene and methanol to remove organic material without altering the mineral composition and oven-dried to a constant weights within ±0.012 g. Samples

used in standard-unstressed MICP tests were cut from parent core plugs having dimension of approximately 1 cm^3 (**Figure 1**). Five of six sides of the cubic samples were then coated with epoxy resin to allow mercury intrusion in one direction. In gas breakthrough experiments, the faulted samples were saturated with deionised water, whereas the mudstone samples pre-covered in a heat-shrink sleeves to preserve their structure, were saturated with brine solution that has been degassed. A brine solution was prepared by dissolving 44.65 grams of potassium chloride (KCl) in one liter of water. This amount was chosen to approximate the ionic strength of a 3.5% sodium chloride (NaCl) solution, which is typical of seawater salinity. The resulting solution had a salinity of 4.27% by weight due to the higher molecular weight of KCl compared to NaCl (Millero et al., 2008). Due to clay mineral hydration, KCl was used as it is known to stabilise clay minerals, preserving the pore geometry of the samples during saturation (Talukdar and Gogoi, 2015).

The samples analysed in this study, including rock type and the experimental methods employed, are summarised in Error! Reference source not found.***Table 1***. A total of 25 rock samples were analysed, consisting of six faulted sandstone and three mudstone samples used in gas breakthrough experiments, five faulted sandstone and two mudstone samples for standard unstressed MICP tests, three faulted sandstone and three mudstone samples for PUCS tests, one faulted sandstone and two mudstone samples for Field's metal injection, and SEM imaging analysis.

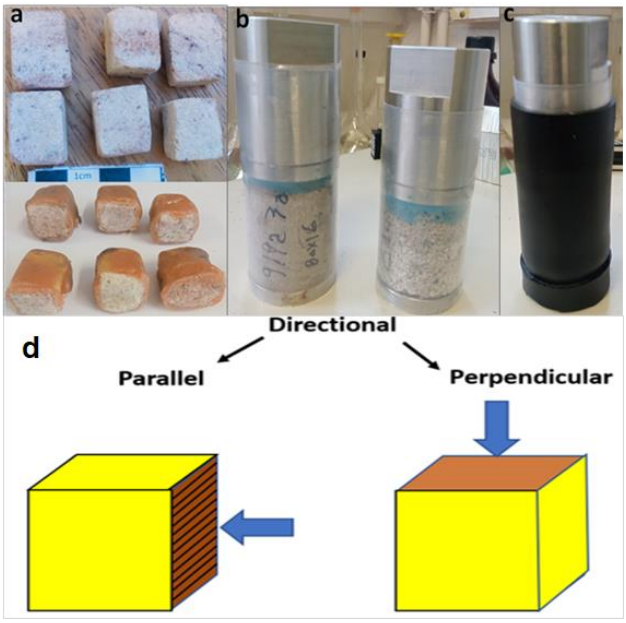

Figure 1: Sample preparation for MICP analysis. (a) Cubic size rock samples used for unstressed MICP analysis coated with epoxy resin. (b-c) Illustrate design arrangements for stressed MICP testing, showing the full core sample sealed in a penetrometer and sleeve with plastic tubing to prevent oil from invading pore structure. (d) Schematics showing directional and non-directional mercury injection in unstressed MICP analysis. The arrows represent the direction of mercury invasion into the samples while the yellow faces represent the faces coated with epoxy resin to prevent the flow of mercury in those directions.

Table 1: *Summary table of rock samples analysed to determine the capillary pressures using different experimental techniques. VE's sample represents the Vale of Eden faulted sandstone, SID the mudstone sample from the Sidmouth Formation, and MMG samples still from Sidmouth Formation but different location*

Sample ID	Method	Sample ID	Method
VE3 (fault)	Gas breakthrough	VE16D (fault)	Standard MICP
VE8 (fault)	Gas breakthrough	VE16E (fault)	Standard MICP
VE9 (fault)	Gas breakthrough	VE14 (fault)	PUCS
VE13(fault)	Gas breakthrough	VE22 (fault)	PUCS
VE15 (fault)	Gas breakthrough	VE24 (fault)	PUCS
VE16 (fault)	Gas breakthrough	SID2 (shale)	Standard MICP
MMG8(shale)	Gas breakthrough	SID2A (shale)	PUCS
MMG11(shale)	Gas breakthrough	SID8A (shale)	PUCS
SID1(shale)	Gas breakthrough	MMG7 (shale)	Standard MICP
VE16A (fault)	Standard MICP	MMG11(shale)	PUCS
VE16B (fault)	Standard MICP	VE7 (fault)	FMI and SEM
VE16C (fault)	Standard MICP	SID2B	FMI and SEM
-	-	MMG3	FMI and SEM

2.2 Gas breakthrough, faulted rock from the Vale of Eden with deionized water

Figure 2 Error! Reference source not found. shows the laboratory experimental setup and schematic diagram used to conduct gas breakthrough experiments on the faulted rock and mudstone samples from the, Vale of Eden and the Mercia Mudstone Group (MMG), respectively. **Figure 2a** was used for the faulted rock samples, consisting of six vertically mounted Hassler™ core holders, each accommodating 3.8 cm diameter, 7.5 cm long core plugs. The holders apply up to 5000 psi (34.5 MPa) confining pressure *via* a Viton sleeve and grooved platens. The upstream side connects to a gas cylinder *via* an Alicat™ pressure controller, while the downstream side leads to a collection bottle. Helium, an inert gas, was used as the non-wetting phase.

Fault rock samples were initially saturated with deionised water and Nuclear magnetic resonance (NMR) scans were used to quantify pore fluid volumes and verify saturation levels. Samples were then mounted in core holders and scanned using computed tomography (CT) under a confining pressure of 1500 psi (10.4 MPa). The CT scans were performed prior to testing and after each pressure increment in order to monitor saturation changes and compare with NMR-derived profiles, enabling analysis of fluid distribution during drainage.

Helium, serving as the non-wetting phase, was injected incrementally from the inlet. After each pressure step, the system was allowed to equilibrate before proceeding.

Produced fluid was collected in pre-weighed bottles and measured. Equilibration times varied depending on the microstructure and composition of sample being tested and typically takes several days. The pressure was increased gradually to avoid overshooting the capillary breakthrough pressure, starting with 1 to 2 psi increments and later increasing to 10 to 20 psi after an initial pressure of 5 psi (Hildenbrand et al., 2002). The confining stress was maintained at constant pressure throughout. Breakthrough was identified by continuous helium flow from the outlet.

2.3 Gas breakthrough on brine saturated mudstones from the MMG

The schematic (**Figure 2b**) of the experimental setup comprised a brine-saturated core sample housed in a core holder, a high-pressure gas injection pump, and a mass balance connected to a glass burette for collecting displaced fluid. An oil layer was added to the burette to prevent evaporation. A Keithley multimeter, configured as a bubble detector with two electrodes across an insulating path, was used to detect gas breakthrough. The system also included pressure gauges and a computer for automated data logging. The multimeter operated at 10 V AC, completing a circuit when conductive brine bridged the electrodes, resulting in a voltage drop. Each sleeved sample was CT scanned under 1500 psi (10.4 MPa) confining pressure at room temperature to verify structural integrity. The NMR scans were performed to quantify water content and confirm full saturation.

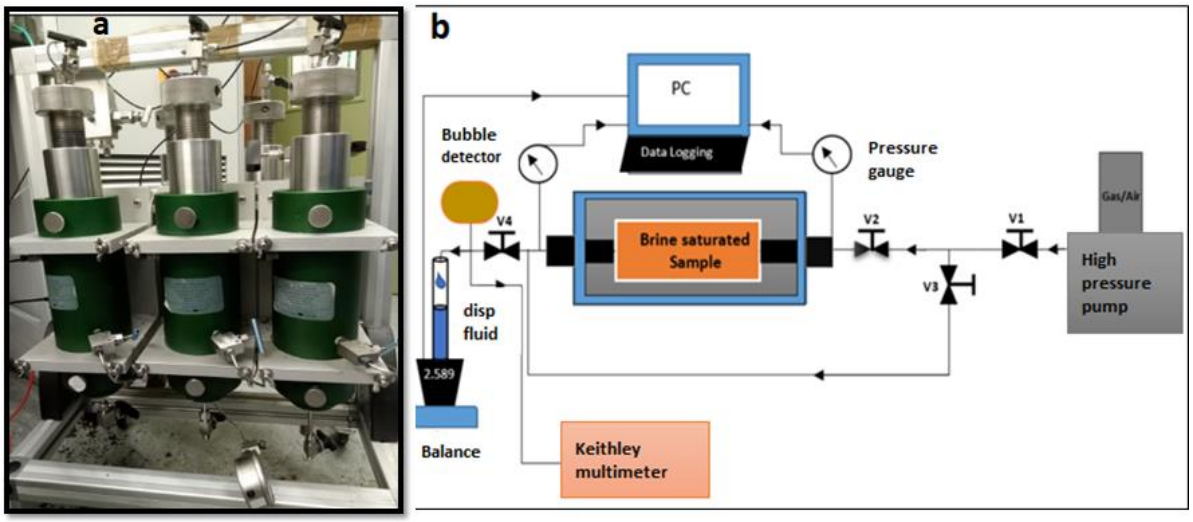

Figure 2. Gas breakthrough experiments: (a) Laboratory setup for faulted sandstone from the Vale of Eden; (b) schematic of the setup used for mudstone samples from the MMG.

In addition, samples were subjected to an increase in confining stress, which resulted in a corresponding increasing in pore pressure indicating that the samples were fully saturated. Both ends of the sample were evacuated to remove trapped air; the downstream was filled with brine up to the sample surface, while the upstream was filled with gas, ensuring no brine was present. Following pressure equilibration, gas

was injected incrementally in 10 psi steps due to the low permeability of the samples. After each step, pressure and displaced fluid mass were monitored until stabilisation, indicating equilibrium. This process was repeated until gas breakthrough was detected, indicated by a sudden voltage change in the bubble detector and a corresponding pressure drop at the downstream. Breakthrough was confirmed by a loss of conductivity, reflected in a negligible voltage signal. The initial increase in collected fluid mass marked the capillary entry pressure, corresponding to the displacement of brine from the largest external pores.

2.5 Mercury injection capillary pressure (MICP) tests

2.5.1 Unconfined MICP

Unconfined MICP tests were performed using a Micromeritics AutoPore IV 9520 porosimeter, equipped with four low-pressure and two high-pressure chambers, capable of applying pressures up to 60,000 psi (414 MPa). The analysis was conducted in two stages. First, samples were sealed in penetrometers using high-vacuum grease and placed in a low-pressure chamber. After evacuation, the penetrometers were backfilled with mercury, and intrusion began at pressures up to 50 psia (345 kPa) to access larger pores. In the second stage, pressure was incrementally increased using a fixed-step method, allowing equilibrium at each step, to force mercury into progressively smaller pores. Maximum pressure reached approximately 60,000 psi (414 MPa) in the high-pressure chamber. Intrusion volume and pressure were continuously recorded. Data were conformance-corrected, and pore size distribution curves were generated using the Laplace-Young equation

$$D = \frac{4\gamma cos\theta}{P_c}, \quad \textbf{(6)}$$

where, D is pore throat diameter (μm), P_c is the applied pressure (psi), γ is the Hg-air surface tension (485 mN/m), θ is the Hg-air-rock contact angle (140°).

2.5.2 Mercury porosimetry under confining stress (PUCS)

Unlike the unstressed MICP approach, the PUCS method measures threshold pressure through the electrical conductivity of mercury spanning across the sample and making electrical contacts with electrodes at both ends of the sample. Stressed MICP tests were conducted on sleeved full core samples under constant effective stress of 2,000 to 7,000 psia (13.8 to 48.3 MPa) to simulate *in-situ* reservoir conditions (Guise et al., 2018).

The resolution of the stressed porosimetry system (PUCS) was comparable to the Autopore IV. Data acquisition and control were automated using custom LabVIEW software developed by InfLogik, while post-processing was performed in Microsoft Excel. The test comprised two phases. In Phase 1, the sleeved sample was placed

between two metal end platens, sealed under vacuum, and filled with mercury from the upstream side. In Phase 2, the assembly was loaded into a pressure vessel and subjected to the target confining stress for 12 hours at a constant temperature of 21°C. Prior to testing, a sample data file containing test parameters and a pore pressure table (defining pressure steps for loading and unloading) was uploaded into the control software. The system was then initialised, and both mercury injection and confining pressure were automatically regulated. Mercury was injected from the top, and at each pressure step, flow velocity was monitored until it dropped below 0.001 $mm^3/cm^2/s$ (10^{-8} m/s), at which point pressure and intrusion volume were recorded. The sample, electrically isolated by grooved platens, initially exhibited high resistivity. When mercury fully spanned the sample length, resistivity dropped significantly, indicating electrical continuity. The corresponding pressure was recorded as the threshold capillary pressure**.**

2.5.3 Field's metal injection

Field's metal is a low-melting-point alloy composed of 32.5% bismuth, 51% indium, and 16.5% tin. Unlike other low-melting alloys such as Wood's metal (which contains toxic cadmium or lead), Field's metal is considered non-toxic under normal use. It has a low vapour pressure, reducing inhalation risks, but can cause skin irritation and burns. When molten, it has an average surface tension of 417 mN/m and is non-wetting, similar to mercury (Zamora et al., 2021). Its melting point of 62°C allows it to be injected as a liquid into the pore network of rock samples. After cooling, the sample is cut and prepared for scanning electron microscopy (SEM) to visualise pore connectivity (Klaver et al., 2017; Yu et al., 2021). Field's metal was selected for this technique due to its non-toxic nature, ease of handling, and low melting point, which reduces the risk of thermal damage. The method enables direct, high-resolution imaging of pore filling and fluid-accessible pathways (Klaver et al., 2017).

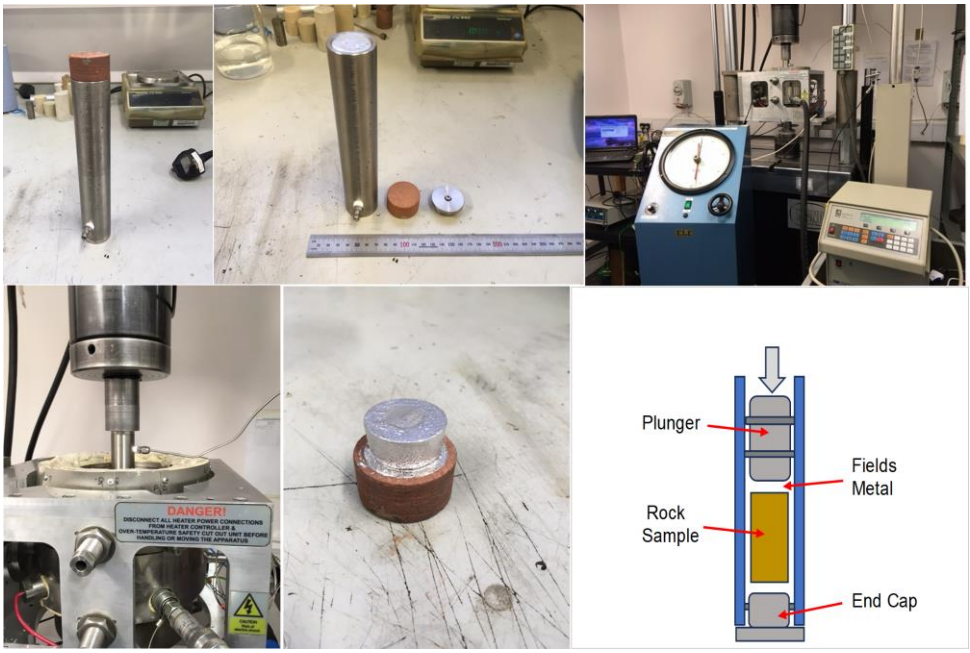

Figure 3. *Laboratory experimental setup and schematic configuration for conducting Field's metal injection in the pore structure of rock samples.*

Field's metal was melted and cast into a cylindrical ingot matching the inner diameter of the pressure cylinder. The rock sample, metal cylinder, and plunger were placed inside the pressure cylinder (**Figure 3**), sealed with a temporary end cap, and heated in an oven at 100°C. Once molten, a C-clamp was used to expel excess air, and the sample was cooled before final sealing. The assembly was then placed in a core holder within a bespoke oven, and axial stress was applied using a hydraulic ram capable of delivering up to 400 psi (2.76 MPa). The experiment began with a confining stress of 700 psi (4.83 MPa). The heating controller was set to 70°C and maintained for one hour to ensure uniform temperature and complete melting. Force, displacement (volume change), and temperature were monitored throughout. Axial stress was increased incrementally until displacement ceased. After reaching maximum stress, the heating was turned off and the system left to cool overnight. The sample was then removed, sliced, and some sections were embedded in epoxy resin and polished following standard SEM preparation procedures. The microstructure was examined using SEM.

3. RESULTS

3.1 Gas breakthrough on faulted rocks from the Vale of Eden

Table 2 presents the pore volumes of the fault rock samples and the percentage of fluid displaced during the drainage experiment, while **Figure 4** shows the capillary pressure curves plotted as a function of saturation. The volume of fluid displaced across the six fault samples is relatively small compared to the total pore volume of each sample. The estimated capillary pressure ranges from 20 psi to 38 psi, whereas the breakthrough pressure range from 25 psi to 40 psi. The breakthrough capillary pressure is identified from the saturation curves as the point of inflection, corresponding to the pressure at which continuous gas production was observed at the downstream end of the sample.

Table 2. *Fault rock samples dimension, pore volumes and the relative percent of fluid displaced*

Sample	VE3	VE8	VE9	VE13	VE15	VE16
Length (cm)	4.77	5.27	4.78	5.16	5.19	5.60
Diameter (cm)	3.78	3.79	3.70	3.79	3.79	3.79
pore volume	4.58	5.47	4.74	6.73	5.54	5.87
Volume of fluid displaced	0.569	1.789	0.716	0.357	0.737	1.637
% of fluid displaced	12.42	32.70	15.09	5.31	13.31	27.89

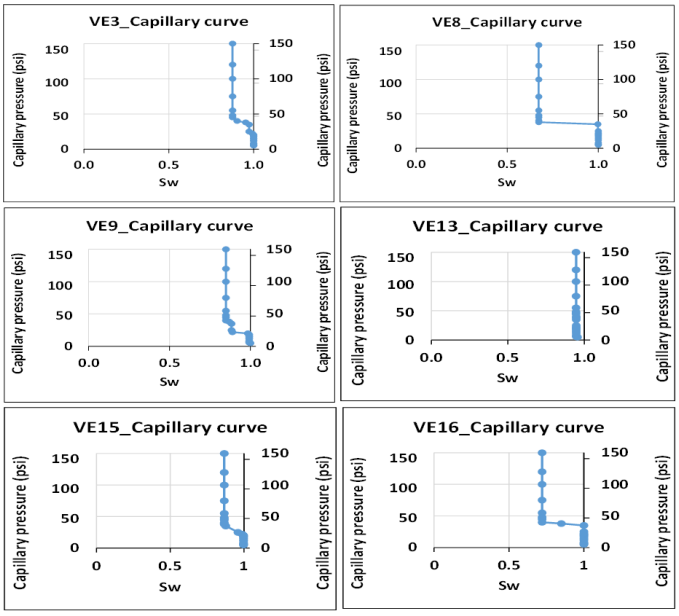

Figure 4. *Capillary pressure curves of fault rock samples as a function of saturation.*

3.2 Gas breakthrough on mudstone from the MMG

Figure 5 presents the gas breakthrough results for the mudstones of the MMG. The plot includes the injection pressure curve, the mass of fluid displaced during the test, and the electrical voltage, all plotted as a function of time (in days). The voltage curve indicates the point of gas breakthrough, marked by a sudden increase in voltage to a maximum of 10 V, due to the poor conductivity of gas as it flows through the circuit.

The curves show that mudstone samples MMG8 and MMG11 exhibit similar breakthrough pressures of 269.8 psi and 271.96 psi, occurring after 49 and 25 days, respectively. By contrast, the Sidmouth sample Sid1 shows a breakthrough pressure of 168 psi after 96 days. These values, along with the volume of fluid displaced and the physical dimensions of the samples, are summarised in **Table 3**.

Table 3. *Summary of table of gas breakthrough for the mudstone of the MMG and Sidmouth Formation.*

Sample ID	*L* (cm)	*D* (cm)	V_p (cm^3)	Porosity (%)	Brine (ρ) (g/cm^3)	V_d (cm^3)	BT (psi)	Duration (day)
MMG8	5.12	3.74	7.59	11.0	1.0219	0.79	269.80	49.0
MM11	4.69	3.86	6.61	12.0	1.0219	0.77	271.96	24.6
SID1	4.07	3.78	9.99	21.9	1.0219	1.96	168.00	96.0

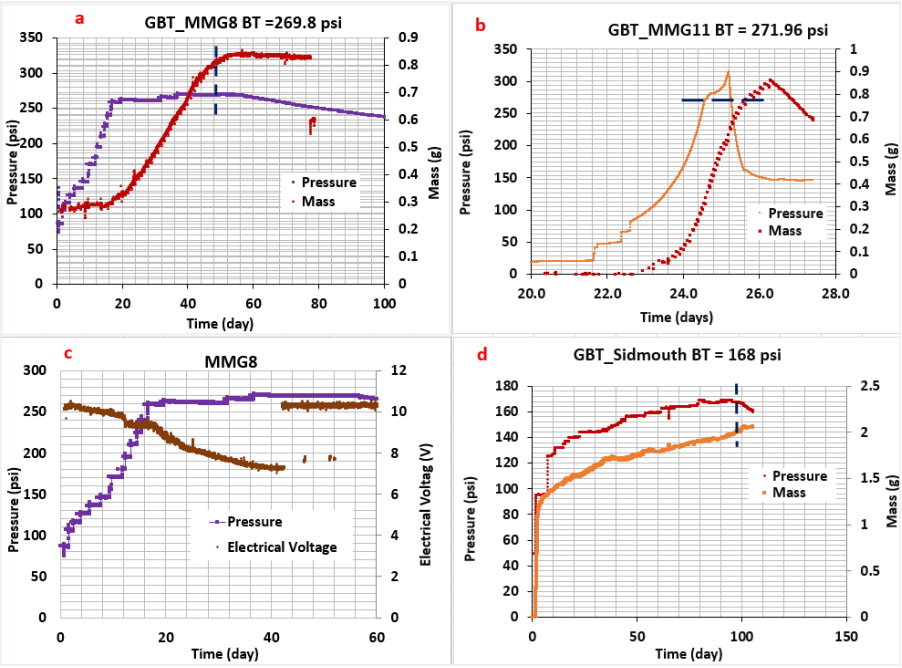

Figure 5. *Gas breakthrough curve on brine saturated mudstones of the MMG.*

3.2.1 Mercury Injection capillary pressure (MICP)

Unstressed MICP on fault rocks of the Vale of Eden

Figure 6 and **Figure 7** present the results of unconfined MICP analysis conducted on five faulted rock samples. In this technique, the threshold pressure is directly estimated from the capillary pressure curves at the point of inflection, which corresponds to the pressure of maximum mercury intrusion (Katz and Thompson, 1986). A complementary approach used involves calculating the derivative of mercury saturation with respect to the logarithm of intrusion pressure, following the method described by Lenormand (2003) defined as:

$$D = \frac{d\left(S_{Hg}\right)}{d\ log(P)}, \quad \textbf{(6)}$$

where D, is the derivative, S_{Hg} is the mercury saturation (%), and P is the intrusion pressure (psi). Plotting the derivative against intrusion pressure produces peak(s) that indicate the pressure ranges where mercury intrusion occurs most rapidly. Plotting this derivative against intrusion pressure produces peak(s) that indicate the pressure ranges where mercury intrusion occurs most rapidly. These peaks correspond to the dominant pores and are closely associated with the capillary threshold pressure in unstressed samples, particularly those exhibiting a unimodal pore throat distribution. The analysis indicates that the unstressed MICP samples have Hg/air capillary threshold pressures ranging from 74.2 psi to 107 psi, with an average value of 96.3 psi (see **Table 4**).

Table 4. *Unconfined MICP capillary threshold pressures for fault rock samples.*

Sample ID	Confining stress (psi)	Threshold pressure (psi)
VE16 (fault)	Unconfined	96.8
VE16A (fault)	Unconfined	107.0
VE16B (fault)	Unconfined	104.4
VE16C (fault)	Unconfined	74.2
VE16D(fault)	Unconfined	99.3

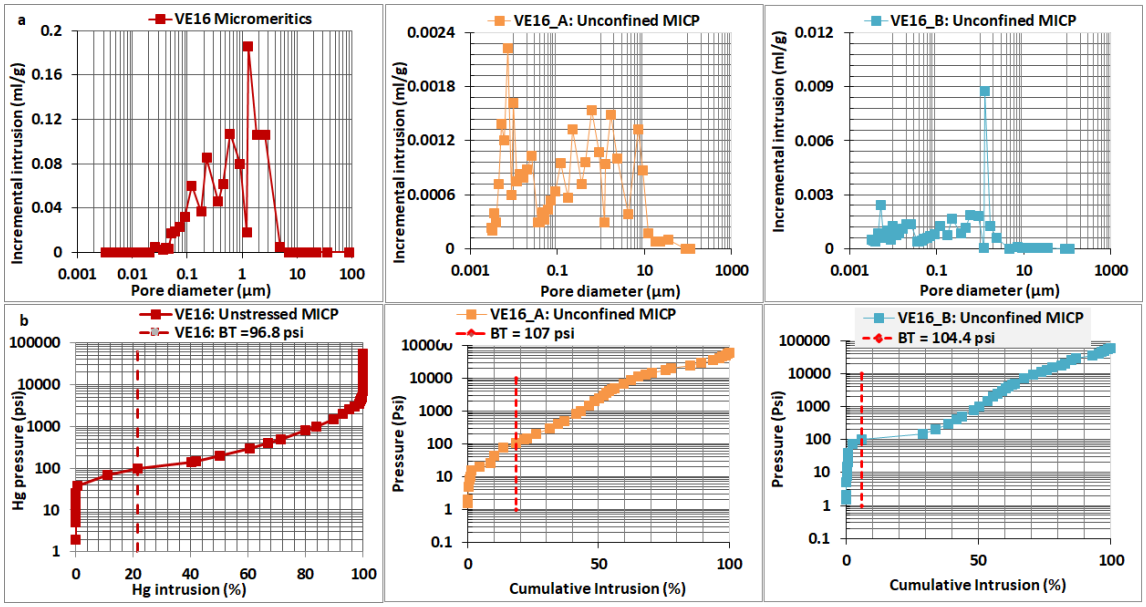

Figure 6. *Unconfined MICP incremental intrusion curves and capillary pressure curves of fault rocks from the Vale of Eden-plot A.*

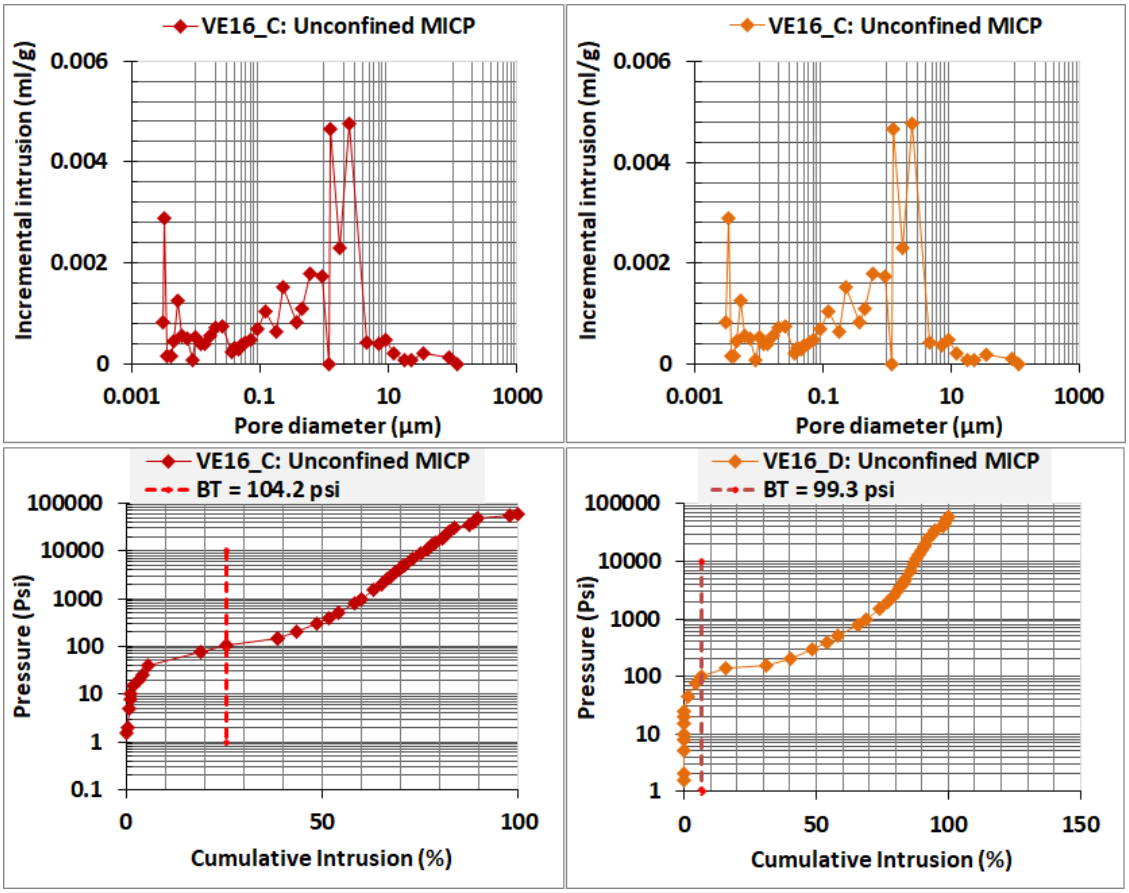

Figure 7. *Unconfined MICP incremental intrusion curves and capillary pressure curves of fault rocks from the Vale of Eden-plot B.*

Stressed MICP (PUCS) on fault rock sample from the Vale of Eden

The capillary threshold pressure of the stressed MICP samples using PUCS was measured through mercury electrical conductivity. This pressure corresponds to the point at which electrical conductivity was first detected across the samples, indicating that mercury had spanned the largest interconnected pathways and established a continuous filament through the sample. Test measurements show that samples VE14 and VE24, subjected to a confining pressure of 500 psi, exhibited threshold pressures of 349 psi and 648 psi, respectively (**Figure 8**). Sample VE22, tested under a confining stress of 7000 psi (48.3 MPa), and recorded a capillary threshold pressure of 1049 psi. However, sample VE14, which had an estimated threshold pressure of 349 psi, did not register electrical contact during the test. Its threshold pressure was therefore inferred using a similar approach to that applied to unconfined samples (i.e., by identifying the point of inflection where mercury accessed the largest interconnected pore spaces). These values are summarised in **Table 5.**

Table 5. *Summary results of stressed MICP using PUCS of the fault rock samples from the Vale of Eden.*

Sample ID	Confining stress (psi)	BT pressure (psi)	Dominant pore (µm)
VE14 (fault)	5000	349	0.518
VE22 (fault)	7000	1049	0.172
VE24 (fault)	5000	648	0.279

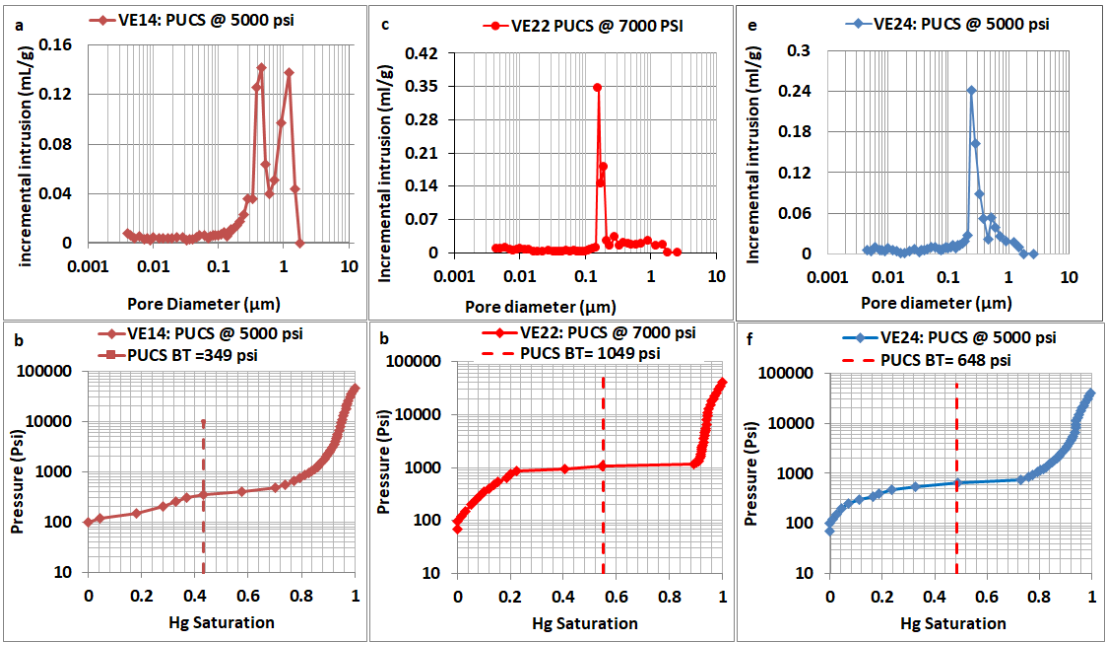

Figure 8. *PUCS MICP incremental intrusion and capillary pressure curves of the fault rock samples from the Vale of Eden.*

Unstressed MICP of the mudstones from the Mercia Mudstone Group (MMG)

The two mudstone samples, SID2 and MMG7, tested using standard MICP (without applied confining stress), exhibited significantly higher threshold pressures compared to the fault sandstone, due to their fine-grained structures. The samples SID2 and MMG7, which display bimodal and unimodal pore size distributions, respectively, recorded threshold pressures of 497.3 psi and 3498 psi, as shown in **Figure 9**. The results are summarised in **Table 6**.

Table 6. *Unstressed MICP threshold pressures for mudstone samples from the Sidmouth Formation of the Mercia Mudstone Group (MMG).*

Sample ID	Confining stress (psi)	Breakthrough pressure (psi)	Dominant pore (µm)
SID2 (Shale)	Unconfined	497.3	0.060
MMG7 (Shale)	Unconfined	3498.5	0.026

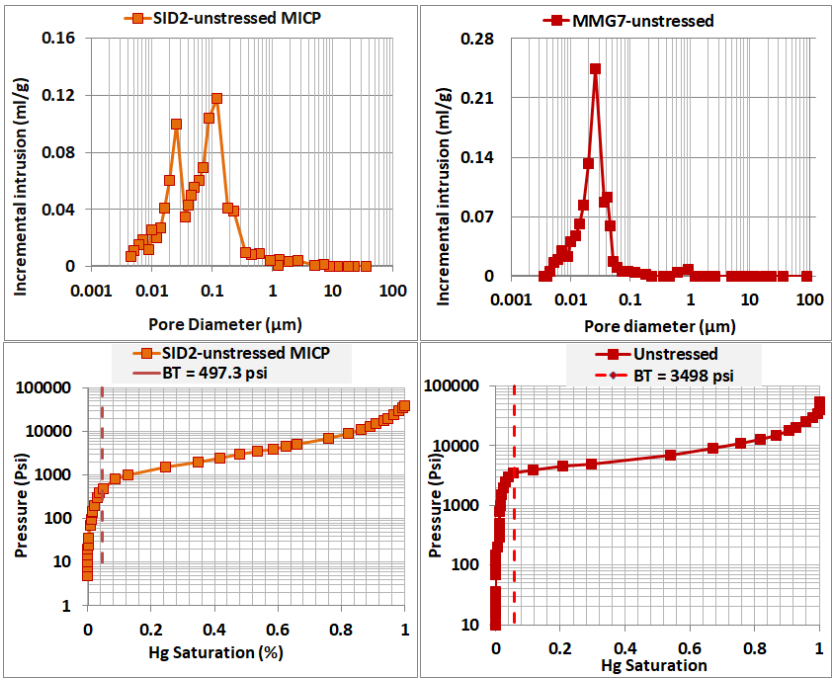

Figure 9. *Unconfined MICP intrusion and capillary pressure curves for the mudstone samples from Sidmouth Formation of the Mercia Mudstone Group (MMG).*

PUCS MICP of the mudstone from the Mercia Mudstone Group

Stressed MICP was conducted on three Sidmouth mudstone samples (SID2A, SID8A, and MMG11) under a confining stress of 2000 psi (13.8 MPa). Compared to the unstressed mudstone samples, which exhibit unimodal and bimodal pore size distributions, the stressed samples showed a multimodal pore size distribution spanning approximately one order of magnitude (**Figure 10**). This likely indicates the

emergence of new pore size populations due to the application of stress. Larger pores (>0.1 μm) are either absent or poorly connected, as evidenced by the very low mercury intrusion volumes. Overall, the stressed mudstone samples exhibit lower mercury intrusion volumes than both the fault rock samples and the unstressed mudstone samples. This suggests a tight formation dominated by mesopores, resulting from the impact of applied stress. Mercury electrical contact was established, and the stressed mudstone samples recorded threshold pressures of 1349 psi, 1649 psi, and 8001 psi for samples SID2A, SID8A, and MMG11, respectively. These high threshold pressure values further support the fine-grained and low-permeability nature of the samples.

Table 7. PUCS mudstone samples from the Mercia Mudstone Group exhibit significant high threshold pressures.

Sample ID	Confining stress (psi)	breakthrough pressure (psi)	Dominant pore (μm)
SID2A (Shale)	2000	1349	0.060
SID8A (Shale)	2000	1649	0.023
MMG11 (Shale)	2000	8001	0.014

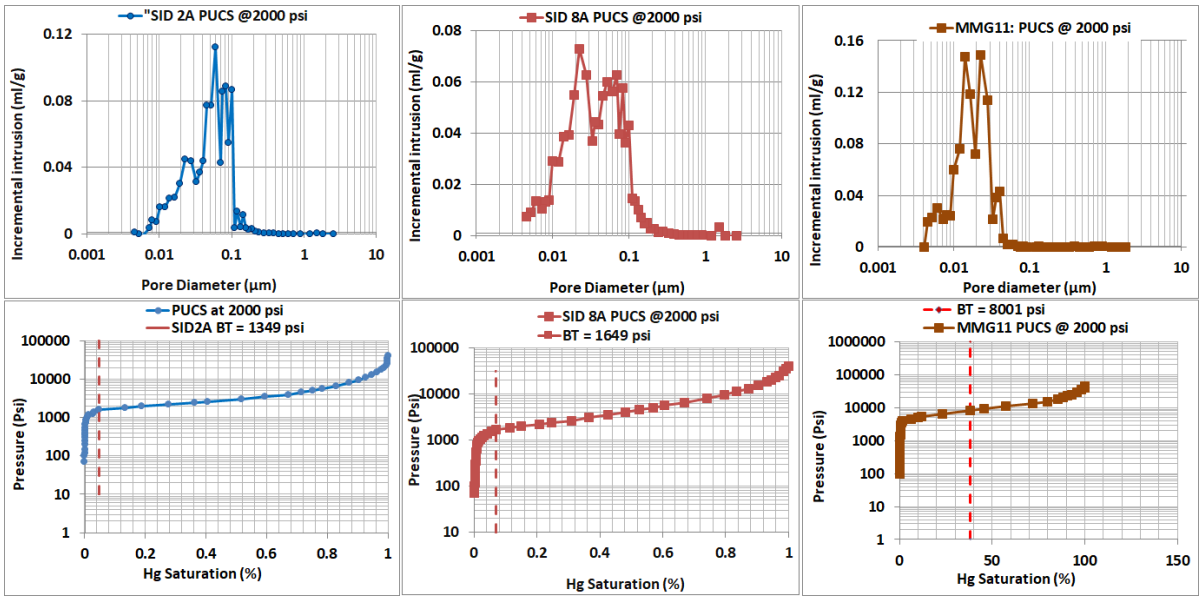

Figure 10. *Intrusion volume and capillary pressure curves of the MMG samples tested using PUCS.*

3.2.2 Field's metal injection and SEM imaging analysis

Molten Field's metal was injected into faulted sandstone from the Vale of Eden and mudstone from the MMG**.** Injection pressure was plotted against cumulative saturation and time (**Figure 11**). For faulted sandstone VE7, intrusion began at about 970 psi (6.7 MPa) and peaked at approximately 5200 psi (35.4 MPa) after over four

hours, after which injection tapered off—indicating most accessible pores were filled. The injection pressure-saturation curve shows gradual filling of larger pores up to 40% saturation, followed by a steeper slope as smaller pores were progressively filled. Saturation peaked at about 51%, then increased further after a sharp pressure drop, suggesting a breakthrough or fracture formation. In mudstone SID2B, pressure was increased in steps from a baseline of 500 psi. Equilibration after each step indicates accommodation of Field's metal. Saturation remained low at lower pressures and reached only about 23% for SID2B and 21% for MMG3 at 3000 psi, which is much lower than for VE7. A sharp rise to about 57% saturation between 3500–4700 psi in MMG3 suggests possible fracture opening, though overall saturation remained lower than in VE7. Estimated threshold pressures were 1568 psi (VE7), 3000 psi (SID2B), and 2500 psi (MMG3).

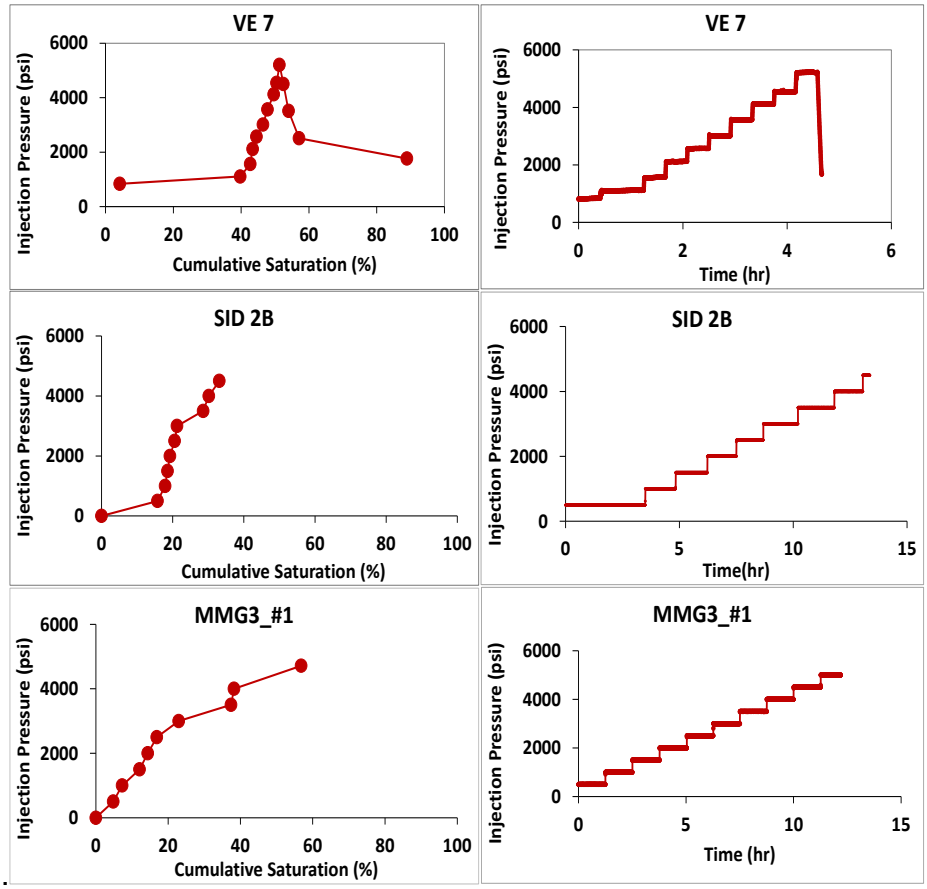

Figure 11. *Field's metal injection into faulted sandstone and mudstone samples, to access and visualised matrix porosity via SEM imaging analysis.*

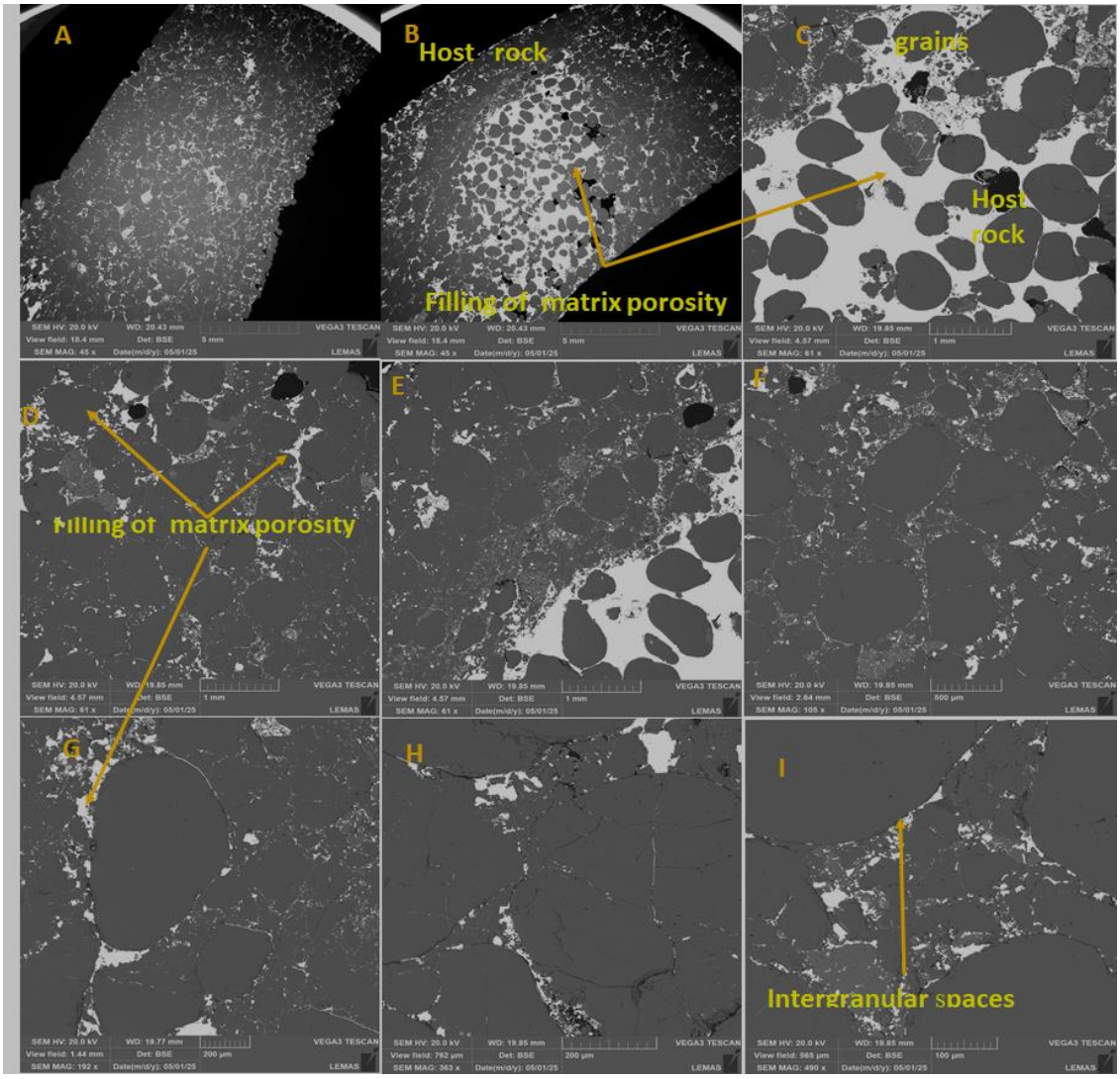

Figure 12. *Scanning Electron Microscopy (SEM) images of faulted sandstone from the Vale of Eden following Field's metal injection. Images (a) and (b) (45× magnification, 5 mm scale) show the general distribution of Field's metal across the sample surface and within intergranular pores. Images (c) – (e) (61× magnification, 1 mm scale) reveal metal infiltration into the porosity of both host and fault rock matrices. Images (f) – (i) (105×, 363×, and 490× magnifications) provide higher-resolution views of Field's metal intrusion into finer intergranular pore structures and pore throats, demonstrating effective penetration of the pore network*

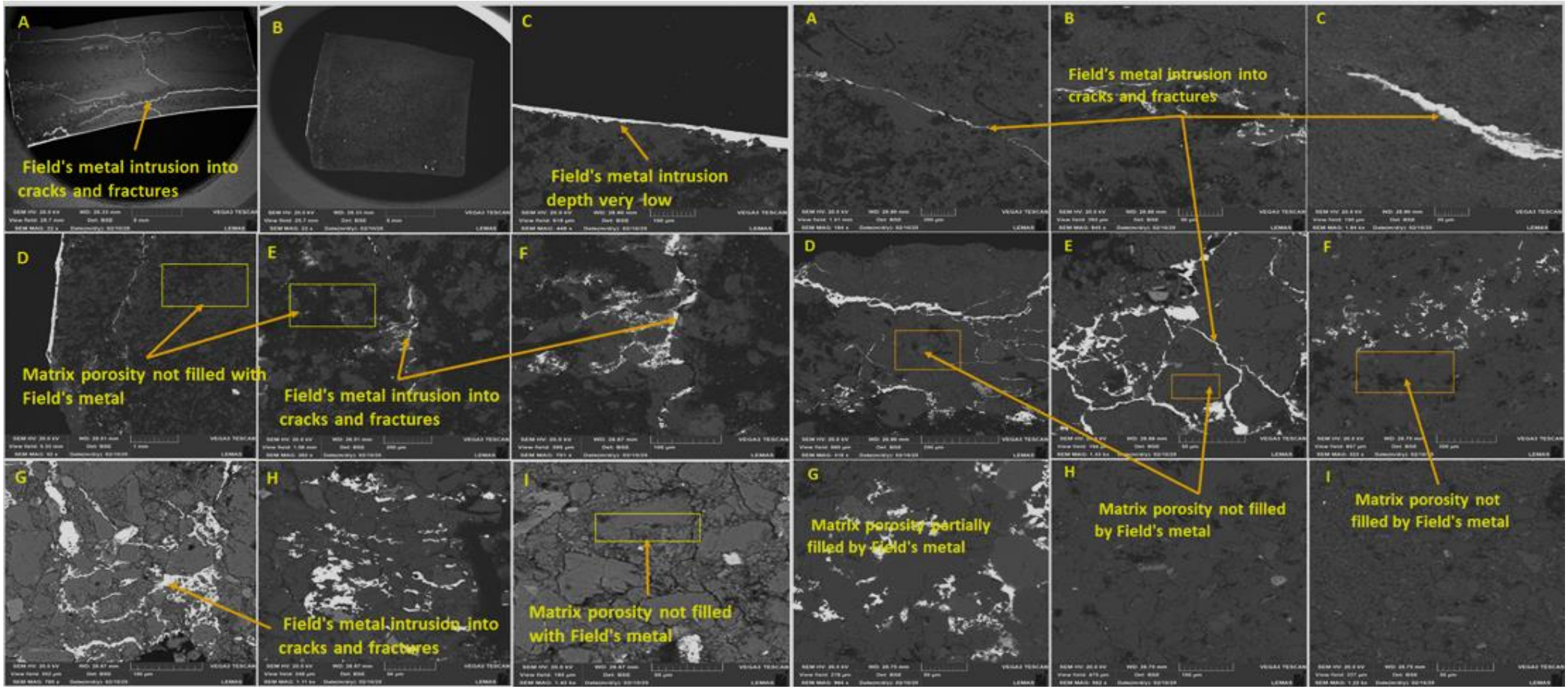

Figure 13. *SEM images showing the distribution of Field's metal in sample MMG3_1. Images C and E, captured at high magnifications (1.84 k× and 1.43 k×, respectively), reveal Field's metal confined to cracks, with no evidence of intrusion into the matrix porosity*

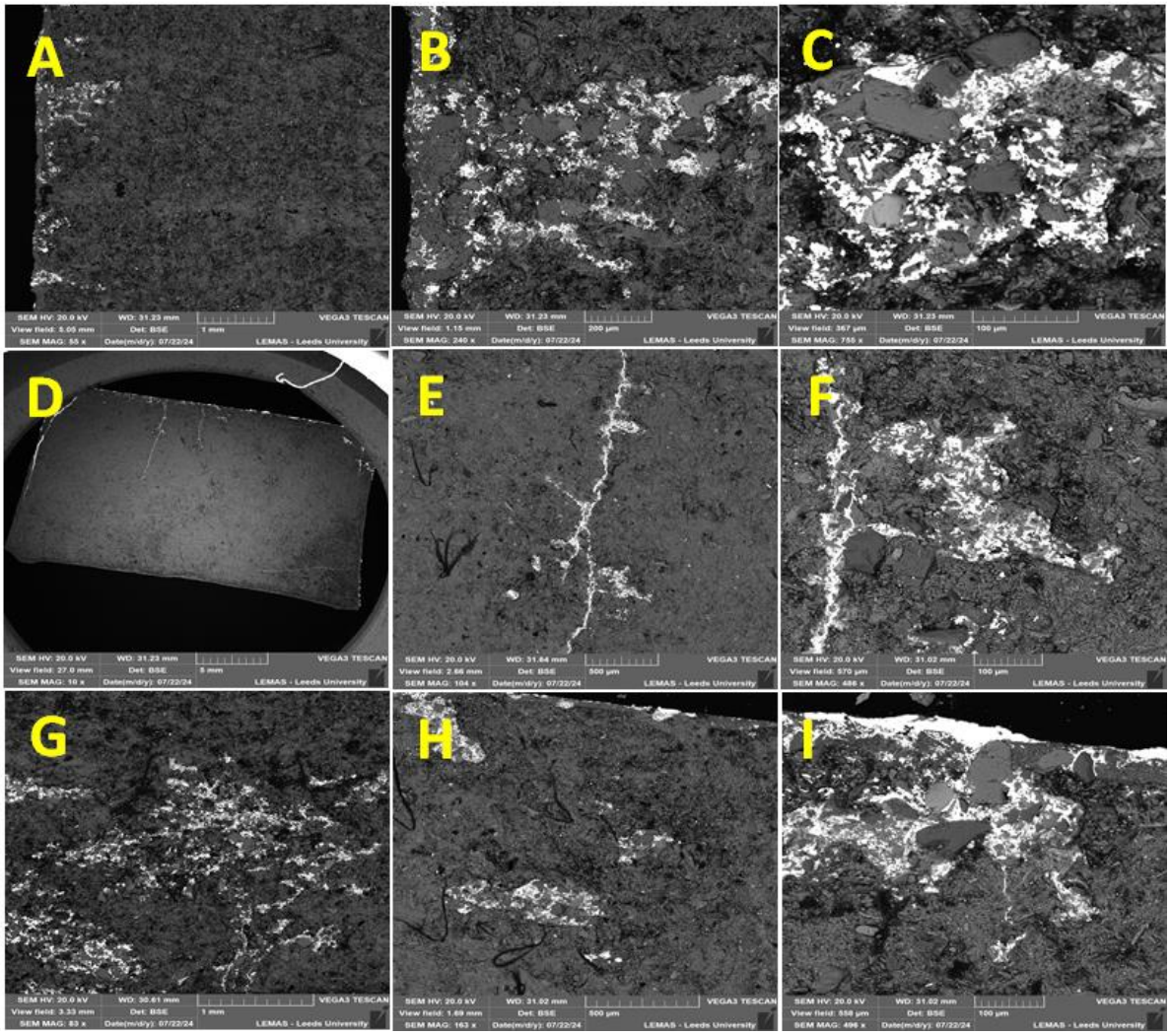

Figure 14. *Field's metal distribution in SID2B_#1 mudstone samples from the Sidmouth Formation. Images (a) – (c) (10×, 55×, and 83× magnifications) provide an overview of Field's metal filling along cracks, with limited penetration depth. Images (d) - (f) (104×, 163×, and 240× magnifications) show more detailed filling of fractures, with no evidence of intrusion into the matrix porosity. Images (g) – (i) present high-resolution views of Field's metal confined to cracks and microfractures, further confirming the absence of matrix-scale intrusion*

4. DISCUSSION

4.1 Comparative analysis of experimental methods and capillary pressures

The MICP data and Field's metal (FM) data must be converted to their air-brine equivalent using appropriate scaling factors to enable meaningful comparison of results between the MICP's and Field's metal injection with those from gas breakthrough conducted in air-brine/water system. **Table 8** presents the conversion factors to translate measurements from Hg-air and FM-air systems to the air-brine system.

Table 8. *Conversion factors used in scaling MICP data and Field's metal (FM) to equivalent air-brine system.*

Parameters	Value	Units
Mercury-air contact angle	140	degrees
Mercury-air interfacial tension	485	mN/m
Air-water/brine-rock contact angle	0	degrees
Air-water/brine interfacial tension	72	mN/m
Field's metal contact angle	141	degrees
Field's metal interfacial tension	417	mN/m
Hydrogen-water/brine IFT	50	mN/m
Hydrogen-water/brine contact angle	30	degrees
Density of deionized water	997	kg/m^3
Density of CO2	500	kg/m^3
Density brine	1021.86	kg/m^3
Gravity	9.81	m/s^2

The conversion is important due to the significant differences in interfacial tensions and wettability among the Hg–air, FM–air, and air–brine systems, which are believed to influence strongly capillary pressure behaviour (Vavra et al., 1992; Daniel and Kaldi, 2009). The conversion was performed using a scaling relationship based on interfacial tension and contact angle ratios, as proposed by Schowalter (1979). The adjusted capillary pressure for the air–brine system was calculated using the following equation:

$$P_{air/brine} = P_{Hg/air}\left(\frac{\gamma_{air/brine} * cos\theta_{air/brine}}{\gamma_{Hg/a} * cos\theta_{Hg/a}}\right), \quad \textbf{(7)}$$

where, $\gamma_{air/brine}$ and $\gamma_{Hg/a}$ are air/brine and mercury/air interfacial tensions, $cos\theta_{air/brine}$ and $cos\theta_{Hg/a}$ are the respective contact angles of air/brine and mercury/air systems, $P_{Hg/a}$ and $P_{air/brine}$ are mercury/air and air/brine capillary pressures respectively.

Table 9 presents the capillary pressures obtained from the gas breakthrough experiments in the air–brine system, while **Table 10** shows the corresponding converted threshold pressures determined using the unconfined MICP, PUCS MICP, and Field's metal methods in the same system. The conversion results indicate that the MICP Hg–air values are approximately 5.16 times greater than the corresponding air–brine values (Purcell, 1949; Thomas et al., 1968), whereas the Field's metal–air-derived values are about 4.02 times higher than those of the equivalent air–brine system.

Table 9. *Summary of the air/brine system capillary pressure in gas breakthrough experiments for both faulted sandstone and mudstone samples.*

Sample	Length (cm)	Diameter (cm)	Confining stress (psi)	Air/brine (BT) (psi)
VE3 (fault)	4.77	3.78	1500	38
VE8 (fault)	5.27	3.79	1500	35
VE9 (fault)	4.78	3.70	1500	38
VE13 (fault)	5.16	3.79	1500	40
VE15 (fault)	5.19	3.79	1500	25
VE16 (fault)	5.60	3.79	1500	38
MMG8 (Caprock)	5.12	3.74	1500	270
MMG1(caprock)	4.37	3.89	1500	272
SID1(caprock)	4.07	3.78	1500	168

Table 10. Summary of MICP and Field's metal data conversion to equivalent air/brine system

MICP data Conversion to air/brine system					
Sample	**Length (cm)**	**Diameter (cm)**	**Confining stress (psi)**	**Hg/air (P_{th}) (psi)**	**Air/brine (P_{th}) (psi)**
VE16 (fault)	1 cm^3	1 cm^3	Unconfined	96.8	18.8
VE16A (fault)	1 cm^3	1 cm^3	Unconfined	107.0	20.7
VE16B (fault)	1 cm^3	1 cm^3	Unconfined	104.4	20.2
VE16C (fault)	1 cm^3	1 cm^3	Unconfined	74.2	14.4
VE16D(fault)	1 cm^3	1 cm^3	Unconfined	99.3	19.2
VE14 (fault)	?	?	5000	349.0	67.6
VE22 (fault)	?	?	7000	1049.0	203.3
VE24 (fault)	?	?	5000	648.0	125.6
SID2 (caprock)	4.95	3.75	Unconfined	497.3	96.4
SID2A (caprock)	6.32	3.72	2000	1349.0	261.4
SID8A (caprock)	5.67	3.75	2000	1649.0	319.6
MMG7 (caprock)	5.07	3.74	Unconfined	3498.5	678.0
MMG11(caprock)	4.69	3.86	2000	8001.0	1551.0
Field's Metal data Conversion to air/brine system					
Sample	**Length (cm)**	**Diameter (cm)**		**FM/air (psi)**	**Air/brine (psi)**
VE7 (Fault rock)	2.83	2.46	-	1570	347
SID2B (Caprock)	2.13	3.76	-	3000	667
MMG3(Caprock)	1.66	3.87	-	2500	555

Figure 15 and **Figure 16** provide a comparative graphical overview of the four methods (i.e., gas breakthrough, unconfined MICP, PUCS MICP, and Field's metal)

alongside data from gas breakthrough experiments conducted on faulted sandstone and undeformed mudstone samples from the Vale of Eden, including the MMG and Sidmouth formations.

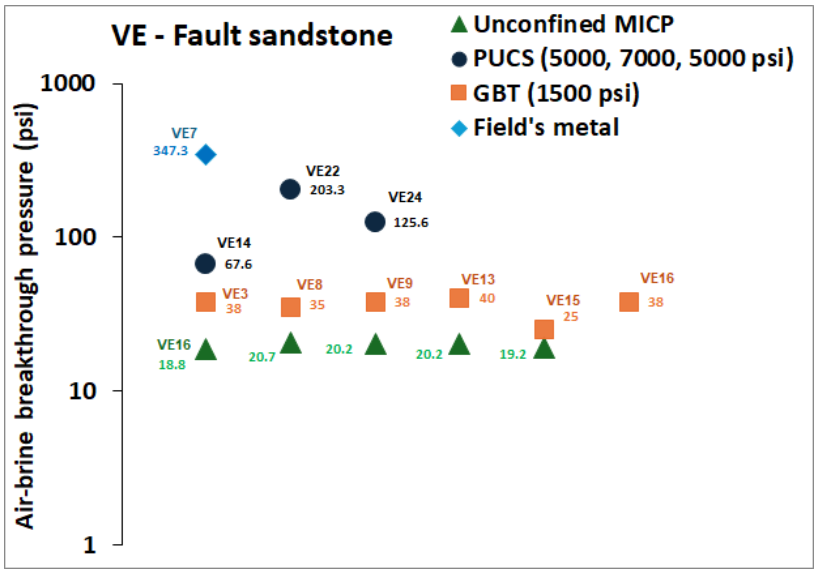

Figure 15. *Comparison of threshold pressures in fault rock samples obtained from gas breakthrough experiments, unconfined MICP, Porosimetry under Confining Stress (PUCS), and Field's metal after conversion to air/brine equivalent system.*

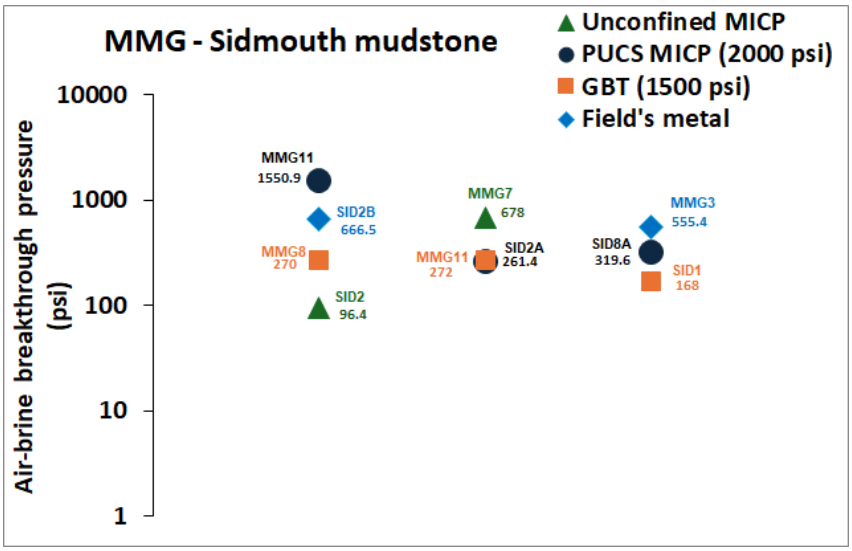

Figure 16. *Comparison of threshold pressures in mudstone samples obtained from gas breakthrough experiments, unconfined MICP, Porosimetry under Confining Stress (PUCS), and Field's metal after conversion to air/brine equivalent system.*

Gas breakthrough experiments on faulted rock and mudstone samples revealed low variability in threshold pressures. Fault sandstones showed tightly clustered values between 35 to 40 psi, with a coefficient of variation (CV) of approximately 4%.

Mudstone samples had threshold pressures centered on 270 psi, except for sample SID1, which recorded a significantly lower threshold value of 168 psi. This is consistent with its' notably higher permeability relative to the other mudstones. The low variation in threshold pressures observed in the faulted rock samples likely reflects similar diagenetic histories, including compaction, cataclastic faulting, and the development of deformation bands, which are processes that reduce pore throat sizes in a consistent manner across the samples (Antonellini and Aydin, 1994).

Overall, the gas breakthrough results for both faulted sandstone and mudstone samples are internally consistent, indicating that the method is reliable and reproducible. It effectively captures the relevant physical properties of the rocks with minimal influence from external disturbances. This consistency further suggests that the method is based on principles applicable across different lithologies.

However, the gas breakthrough results are neither consistent with nor directly comparable to those from MICP and Field's metal-derived values in the air–brine system. In fault rock samples, the PUCS method produced significantly higher and more variable threshold pressures (68 to 203 psi), while the unconfined MICP yielded much lower values, averaging around 19 psi, which is approximately half the values obtained *via* gas breakthrough. For mudstones, unconfined MICP results (MMG7 and SID2) showed high variability, with a 75% coefficient of variation, suggesting a potential outlier — likely the higher value from MMG7. The PUCS-derived values for mudstones ranged from 261 psi to 1551 psi, with over 80% variation, more than three times the gas breakthrough values. These discrepancies suggest that the standard unconfined MICP may underestimate threshold pressures due to the absence of confining stress, while the PUCS method may overestimate them under applied stress. Additionally, MICP results, both unconfined and PUCS, exhibit greater internal variability compared to the more consistent gas breakthrough method.

Moreover, like the unconfined MICP approach, the threshold pressures for Field's metal injection were estimated arbitrarily from saturation–pressure curves, typically at the inflection point. These pressures were significantly higher than those obtained *via* gas breakthrough for both rock types, and higher than those from MICP tests on sandstone samples. They were also generally higher than MICP-derived values for mudstone, except for sample MMG11, which showed the highest threshold pressure under stressed MICP conditions. Despite this, Field's metal results showed good internal consistency, with a coefficient of variation of approximately 9% across samples. Overall, Field's metal injection tends to yield higher threshold pressures than both gas breakthrough and MICP methods, indicating that its results may not be comparable directly with those techniques.

In summary, the threshold pressure measured or estimated from the four methods—gas breakthrough, unconfined MICP, PUCS MICP, and Field's metal injection—show that gas breakthrough offers high internal consistency but lacks comparability with MICP and Field's metal methods. The MICP results were variable and inconsistent across samples. Field's metal injection showed high internal consistency and generally yielded higher threshold pressures than both gas breakthrough and MICP, with limited variability across samples. The discrepancies in threshold pressures across the four experimental methods can be attributed to several inherent factors, which are outlined and discussed in the following section.

4.2 Underlying causes of variation in threshold pressure across methods

4.2.1 Uncertainty in measurement approaches

The observed variation in threshold pressure across the four measurement techniques can be largely attributed to the intrinsic or inherent uncertainties in each measurement approach.

In the gas breakthrough technique, the capillary breakthrough pressure is typically assumed at the onset of continuous gas flow from the downstream end of the sample, a condition that is sensitive and influenced by subjective interpretation. This approach may fail to detect early micro-scale gas migration, leading to potential underestimation of the true threshold pressure, particularly in low-permeability formations. In unconfined MICP and Field's metal injection, threshold pressures are inferred from the saturation-pressure curves, often at the point of inflections (Katz and Thompson, 1986). This approach may likely introduce unconscious user bias and variability (Schlomer and Krooss 1997), as curve interpretation can be affected by sample heterogeneity and surface irregularity, though conformance correction may have been applied.

Moreover, PUCS MICP measurement is based on establishment of mercury electrical contact across the sample to detect threshold pressure. However, in low-to-ultra-low permeability or poorly connected pore structure, contact may not be established, as was in the case of sample VE16 (the faulted samples with deformation bands) leading to incomplete or unreliable data and possible interpretation of the threshold pressure using another method. Comparative studies have shown that MICP, particularly the unconfined method, underestimates threshold pressure (Guise et al., 2017) when compared to dynamic gas-water displacement methods especially under *in-situ* reservoir conditions. These methodological limitations highlight the significant importance of cross-validation and careful interpretation when comparing threshold/breakthrough pressures across various experimental methods.

4.2.2 Lack of standardised conversion factors in Field's metal injection

Accurate estimation of threshold pressures in MICP and Field's metal injection methods relies heavily on the ability to convert measured values to an equivalent air–brine system using reliable formulas and conversion factors. For MICP, this typically involves applying the Young–Laplace equation, which relates capillary pressure to interfacial tension, contact angle, and pore radius. For Field's metal, the challenge is greater due to the lack of standardized interfacial parameters. Beyond the uncertainty in identifying inflection points on saturation–pressure curves, converting Field's metal–air data to an air–brine equivalent requires accurate values for interfacial tension and contact angle between Field's metal, air, and rock surfaces. These parameters have not been directly measured for geological materials. The closest available data are from Zamora et al. (2021), who reported values for Field's metal–nitrogen–glass systems at temperatures above 80°C. Relying on such approximations introduces significant uncertainty, potentially leading to under- or overestimation of threshold pressures. This highlights the need for direct measurement or calibration of interfacial properties specific to geological systems to improve the reliability of threshold pressure estimates.

4.2.3 Failure of mercury to enter pore space: Evidence from Field's metal injection

Mercury Injection Capillary Pressure (MICP) analysis is widely used to characterise pore size distribution and estimate capillary entry pressure in porous media (Olson & Grigg, 2008). The technique operates on the principle that mercury, a non-wetting fluid, intrudes into the pore network under increasing pressure (Shafer & Neasham, 2000). However, in low-permeability, clay-rich-shale formations, MICP pressure–intrusion data may not accurately reflect true pore invasion. Mercury may not penetrate the pore structure, as reported by Hildenbrand & Urai (2003) and Klaver et al. (2015; 2017). Instead, measurements can be significantly influenced by rock matrix compressibility, leading to overestimated threshold pressures due to compressibility artefacts, manifesting as apparent increases in intrusion volume misinterpreted as pore filling (Klaver et al., 2015).

This phenomenon was diligently investigated in the present study using Field's metal injection followed by Scanning Electron Microscopy (SEM) imaging. The results showed that Field's metal effectively intruded fault rock samples, achieving saturation levels near 90% (**Figure 11**, VE7). Some SEM images (**Figure 12**) confirmed widespread distribution of Field's metal within matrix porosity and intergranular pore spaces. These findings suggest that the threshold pressure estimated in the stressed MICP (PUCS) likely reflect true values and correspond to actual pore invasion. Any variation observed in the faulted rock threshold value may reflects the structural heterogeneity of the samples, indicating that MICP provided a valid representation of pore structure and capillary entry pressure in these formations.

By contrast, mudstone samples exhibited markedly different behaviour. While pressure–saturation curves in MICP suggested mercury intruded mudstone porosity, SEM analysis revealed that Field's metal (acting as a proxy for mercury) primarily filled pre-existing or stress-induced microfractures, with minimal intrusion into matrix pores (**Figure 13** and **Figure 14**). This indicates that mudstone pore throats are extremely fine and largely inaccessible to metal intrusion. Consequently, elevated threshold pressures from stressed MICP tests in mudstones likely reflect sample compressibility rather than true pore invasion. This explains the significant discrepancy between MICP-derived and gas breakthrough threshold pressures. Although research on Field's metal for pore connectivity visualization is limited, similar alloys like Wood's metal have been used in several studies. Klaver et al. (2015) demonstrated that Wood's metal primarily filled cracks and microfractures in formations such as Opalinus Clay and Haynesville Shale, with limited matrix intrusion. In Bossier Shale, localized pore filling indicated heterogeneous connectivity, while Boom Clay showed more extensive intrusion due to higher silt content. Klaver et al. (2017) further showed that in tight sandstones, metal intrusion was localised and governed by pore connectivity, with SEM images revealing preferred flow paths such as microfractures and intergranular pores. Moreover, Hildenbrand & Urai (2003) found that molten Wood's metal did not significantly penetrate mudstone matrices, attributing this to clay fabric deformation under high pressure during mercury intrusion. This aligns with observations in this study, where multiple peaks in intrusion curves suggest pore structure collapse and reorientation, forming new pore populations with bottleneck geometries that hinder mercury intrusion.

These findings, supported by existing literature, highlight the limitations of MICP in characterising pore size distribution and threshold pressures in low-permeability rocks. While MICP is effective for permeable formations like fault sandstones, its reliability diminishes in mudstones, where apparent saturation increases may result from microfractures filling and matrix compressibility under confining pressure.

4.2.4 The impact of heterogeneity on sweep efficiency

Heterogeneity significantly influences sweep efficiency during drainage in porous media. Variations in pore size distribution and permeability lead to non-uniform flow paths, resulting in early gas breakthrough and poor displacement of the resident wetting phase (Zhang et al., 2021). While MICP analysis offers valuable insights into pore structure under quasi-static conditions, it remains unclear whether MICP tests adequately account for dynamic phenomena such as capillary fingering, commonly observed in gas displacement experiments. Although preferential intrusion of Field's metal into fractures and microcracks may suggest capillary fingering, this behaviour is yet to be observed in mercury-based MICP tests. Conversely, the gas

breakthrough method captures the interplay between viscous and capillary forces during drainage, making it more sensitive to heterogeneity-induced fingering and bypassing (Lei et al., 2022). The discrepancies between MICP-derived and gas breakthrough threshold pressures in fault rocks can thus be attributed to heterogeneity effects.

In more details, **Table 2** presents the total fluid volume and percentage of pore volume displaced during gas breakthrough tests on six faulted rock samples. The displaced volumes were significantly lower than the total pore volumes, indicating low sweep efficiency likely caused by sample heterogeneity. Preferential flow paths, driven by heterogeneity, result in uneven and incomplete fluid displacement (Zhang et al., 2021). **Table 11** listed MICP-analysed fault rock and mudstone samples along with their heterogeneity indices, calculated using the coefficient of variation (CV)—the ratio of standard deviation to mean pore diameter (Koch & Link, 1971). Although heterogeneity indices were not directly computed for the six fault rock samples tested *via* gas breakthrough, sample VE16, cored from the same parent rock and analysed under isostatic mercury compression, exhibited a high CV of 2.93. This supports the interpretation that low fluid recovery during gas breakthrough is linked to poor sweep efficiency and preferential flow, both driven by high heterogeneity.

Table 11. *Summary of MICP analysed fault rock and mudstones sample's heterogeneity indices and level of saturation at breakthrough pressure, showing samples analysed under isostatic mercury compression exhibited lower saturation at breakthrough pressure.*

Sample	Sample description	Confining stress (psi)	Heterogeneity index
VE16	Fault rock	Unconfined	2.93
VE14	Fault rock	5000	1.62
VE22	Fault rock	7000	1.73
VE24	Fault rock	5000	1.73
SID2	Mudstone	Unconfined	2.23
SID2A	Mudstone	2000	1.73
SID8A	Mudstone	2000	1.73
MMG7	Mudstone	Unconfined	2.95
MMG11	Mudstone	2000	1.62

4.3 Implications for validity of methods

This study employed four experimental methods: (i) gas breakthrough, (ii) unconfined MICP, (iii) PUCS MICP, and (iv) SEM imaging following Field's metal injection in order to determine threshold pressures in faulted sandstone (with deformation bands) and mudstone samples. The aim was to estimate capillary threshold pressures and assess the sealing capacities of these lithologies.

The gas breakthrough method demonstrated strong internal consistency across both rock types, indicating reliable capture of capillary threshold pressures. Its reproducibility across heterogeneous samples supports its robustness for evaluating sealing capacity in diverse geological settings. However, in faulted sandstones, intrinsic heterogeneity and preferential flow pathways may lead to early gas breakthrough via viscous fingering, potentially underestimating true threshold pressures. Field's metal injection also showed high internal consistency, with a low coefficient of variation (~9%). However, its threshold pressure values were consistently higher than those from gas breakthrough and MICP, likely due to the absence of standardized conversion factors for the Field's metal–rock system.

The MICP results exhibited significant internal variability and discrepancies across both fault rocks and mudstones. These inconsistencies are attributed to factors such as incomplete pore invasion, rock compressibility effects, pore structure heterogeneity, and irreducible water saturation. The SEM imaging following Field's metal injection revealed that mercury did not intrude matrix porosity in clay-rich mudstones, instead filling fractures and microcracks. This suggests that MICP may misrepresent pore structure in such formations, leading to inaccurate threshold pressure estimates.

5. CONCLUSIONS AND RECOMMENDATIONS

This study demonstrates that although Mercury Injection Capillary Pressure (MICP) remains a widely used and effective technique for characterising pore structures in permeable formations, its reliability declines markedly in low-permeability, clay-rich rocks such as shales and mudstones. In these lithologies, MICP often misrepresents capillary threshold pressures because it cannot access matrix porosity and is highly sensitive to fracture-dominated pathways. These limitations create significant challenges for accurately assessing fluid flow properties, which are critical for applications such as subsurface fluid storage and nuclear waste disposal.

Given these constraints, method selection must be tailored to formation characteristics, and caution is essential when interpreting MICP data from tight, heterogeneous rocks. To address this gap, we recommend developing an alternative system that can measure key shale properties such as permeability and capillary threshold pressure with greater accuracy, speed, and throughput. Such a system should enable dynamic, pore-scale visualisation of fluid displacement and simulate realistic subsurface conditions, making it a promising solution for evaluating sealing capacity in energy transition and waste containment scenarios.

REFERENCES

Antonellini, M. and Aydin, A.. 1994. *Effect of faulting on fluid flow in porous sandstones: petrophysical properties. AAPG bulletin*, 78(3), pp.355-377.

Bonazzi, A., Morvillo, M., Im, J., Jha, B. and de Barros, F.P.J.. 2021. *Relative impacts of permeability heterogeneity and viscosity contrast on solute mixing. Physical Review Fluids*, 6(6), p.064501.

Brown, A.A.. 2015. PS Interpreting Permeability from Mercury Injection Capillary Pressure Data.

Bust, V.K., Majid, A.A., Oletu, J.U. and Worthington, P.F.. 2013. *The petrophysics of shale gas reservoirs: Technical challenges and pragmatic solutions. Petroleum Geoscience*, 19(2), pp.91-103.

Chen, B., Li, Q., Tan, Y., Yu, T., Li, X. and Li, X.. 2024. *Experimental measurements and characterization models of caprock breakthrough pressure for CO2 geological storage. Earth-Science Reviews*, 252, p.104732.

Chen, M., Li, Q., Cheng, L., Wang, X., Lyu, C. and Fan, Q.. 2021. *A Study to Investigate the Viscosity Effect on Micro-Confined Fluids Flow in Tight Formations Considering Fluid–Solid Interaction. Frontiers in Earth Science*, 9, p.795842.

Claret, F., Marty, N. and Tournassat, C.. 2018. *Modeling the Long-term Stability of Multi-barrier Systems for Nuclear Waste Disposal in Geological Clay Formations. Reactive transport modeling: applications in subsurface energy and environmental problems*, pp.395-451.

Daniel, R.F. and Kaldi, J.G.. 2009. Evaluating seal capacity of cap rocks and intraformational barriers for CO2 containment.

Davudov, D., Moghanloo, R.G. and Lan, Y.. 2018. *Evaluation of accessible porosity using mercury injection capillary pressure data in shale samples. Energy & Fuels*, 32(4), pp.4682-4694.

Eke, P.E., Naylor, M., Haszeldine, S. and Curtis, A.. 2011, September. CO2 leakage prevention technologies. In SPE Offshore Europe Conference and Exhibition (pp. SPE-145263). SPE.

Ewy, R.T.. 2015. *Shale/claystone response to air and liquid exposure*, and implications for handling, sampling and testing. International Journal of Rock Mechanics and Mining Sciences, 80, pp.388-401.

Fisher, Q., Kaminskaite, I. and del Pino Sanchez, A.. 2023. *Shale barrier performance in petroleum systems: implications for CO2 storage and nuclear waste disposal. Geoenergy*, 1(1), pp.geoenergy2023-006.

Guise, P., Grattoni, C.A., Allshorn, S.L., Fisher, Q.J. and Schiffer, A. 2018. *Stress sensitivity of mercury-injection measurements. Petrophysics*, 59(01), pp.25-34.

Hildenbrand, A. and Urai, J.L.. 2003. *Investigation of the morphology of pore space in mudstones—first results. Marine and Petroleum Geology*, 20(10), pp.1185-1200.

Jenkins, C., Pestman, P., Carragher, P. and Constable, R.. 2024. *Long-term risk assessment of subsurface carbon storage: analogues*, workflows and quantification. Geoenergy, 2(1), pp. geoenergy2024-014.

Jennings, J.B.. 1987. *Capillary pressure techniques: application to exploration and development geology. AAPG Bulletin*, 71(10), pp.1196-1209.

Klaver, J., Hemes, S., Houben, M., Desbois, G., Radi, Z. and Urai, J.L.. 2015. *The connectivity of pore space in mudstones: insights from high‐pressure Wood's metal injection*, BIB-SEM imaging, and mercury intrusion porosimetry. Geofluids, 15(4), pp.577-591.

Klaver, J., Schmatz, J. and Urai, J.L.. 2017, June. Liquid Metal Injection: A novel tool to investigate connected porosity and transport pathways in unconventional reservoirs. In SPE Europec featured at EAGE Conference and Exhibition? (p. D041S009R003). SPE

Le Guen, Y., Le Gouevec, J., Chammas, R., Gerard, B., Poupard, O., Van Der Beken, A. and Jammes, L.. 2009. *CO2 storage: managing the risk associated with well leakage over long time scales. SPE Projects*, Facilities & Construction, 4(03), pp.87-96.

Lei, W., Lu, X., Liu, F. and Wang, M.. 2022. *Non-monotonic wettability effects on displacement in heterogeneous porous media. Journal of fluid mechanics*, 942, p.R5.

Li, Y. and Yu, Q.. 2020. *Rock-core scale modeling of initial water saturation effects on CO2 breakthrough pressure in CO2 geo-sequestration. Journal of Hydrology*, 580, p.124234.

Liu, H.H.. 2014. *Non-Darcian flow in low-permeability media: key issues related to geological disposal of high-level nuclear waste in shale formations. Hydrogeology Journal*, 22(7), pp.1525-1534.

Lohr, C.D. and Hackley, P.C.. 2018. *Using mercury injection pressure analyses to estimate sealing capacity of the Tuscaloosa marine shale in Mississippi*, USA: Implications for carbon dioxide sequestration. International Journal of Greenhouse Gas Control, 78, pp.375-387.

Olson, R.K. and Grigg, M.W.. 2008. Mercury injection capillary pressure (MICP) a useful tool for improved understanding of porosity and matrix permeability distributions in shale reservoirs. Search and Discovery Article 40322.

Olson, R.K. and Grigg, M.W.. 2008. Mercury injection capillary pressure (MICP) a useful tool for improved understanding of porosity and matrix permeability distributions in shale reservoirs. Search and Discovery Article 40322.

Pasala, S.M., Forster, C.B., Deo, M. and Evans, J.P.. 2013. *Simulation of the impact of faults on CO 2 injection into sandstone reservoirs. Geofluids*, 13(3), pp.344-358.

Pokharel, T.R. and Rijal, H.B.. 2021. *Energy transition toward cleaner energy resources in Nepal. Sustainability*, 13(8), p.4243.

Purcell, W.R.. 1949. *Capillary pressures-their measurement using mercury and the calculation of permeability therefrom. Journal of Petroleum Technology*, 1(02), pp.39-48.

Purcell, W.R.. 1950. *Interpretation of capillary pressure data. Journal of Petroleum Technology*, 2(08), pp.11-12.

Rashid, F., Glover, P.W.J., Lorinczi, P., Hussein, D., Collier, R. & Lawrence, J.. 2016. *Permeability prediction in tight carbonate rocks using capillary pressure measurements. Marine and Petroleum Geology*, 68(Part A), pp. 536–550. doi: https://10.1016/j.marpetgeo.2015.10.005 .

Schlomer, S. and Kroose, B.M. 1997. *Experimental characterisation of the hydrocarbon sealing efficiency of cap rocks. Marine and Petroleum Geology*, 14, 565-580, https://doi.org/10.1016/S0264-8172(97)00022-6

Schowalter, T.T.. 1979. *Mechanics of secondary hydrocarbon migration and entrapment. AAPG bulletin*, 63(5), pp.723-760.

Shafer, J. and Neasham, J.. 2000, October. Mercury porosimetry protocol for rapid determination of petrophysical and reservoir quality properties. In International Symposium of the Society of Core Analysts (pp. 18-22). Fredericton, NB, Canada: Society for Core Analysts.

Siqveland, L.M. and Skjæveland, S.M.. 2021. *Derivations of the Young-Laplace equation. Capillarity*, 4(2), pp.23-30.

Thomas, L.K., Katz, D.L. and Tek, M.R. 1968. *Threshold pressure phenomena in porous media. Society of Petroleum Engineers Journal*, 8(02), pp.174-184.

Thomas, L.K., Katz, D.L. and Tek, M.R. 1968. *Threshold pressure phenomena in porous media. Society of Petroleum Engineers Journal*, 8(02), pp.174-184.

Toulhoat, P.. 2002. *Confinement and migration of radionuclides in a nuclear waste deep repository. Comptes Rendus Physique*, 3(7-8), pp.975-986.

Washburn, E.W.. 1921. *Note on a method of determining the distribution of pore sizes in a porous material. Proceedings of the National Academy of Sciences*, 7(4), pp.115-116.

Washburn, E.W.. 1921. *The dynamics of capillary flow. Physical review*, 17(3), p.273.

Wehbi, H.. 2024. *Powering the future: an integrated framework for clean renewable energy transition. Sustainability*, 16(13), p.5594.

Zamora, R., Martínez-Pastor, J. and Faura, F.. 2021. *Thermal*, viscoelastic and surface properties of oxidized Field's metal for additive microfabrication. Materials, 14(23), p.7392.

Zamora, R., Martínez-Pastor, J. and Faura, F.. 2021. *Thermal*, viscoelastic and surface properties of oxidized Field's metal for additive microfabrication. Materials, 14(23), p.7392.

Zhang, H., Xiao, L., Wang, M., Ge, X., Hu, X. and Tan, W.. 2022. *Comprehensive Experimental Study on the Gas Breakthrough Pressure and Its Implication for the Reservoir Performance. Lithosphere. 2022(Special 13)*, p.9260593.

Zhang, J., Zhang, H., Lee, D., Ryu, S. and Kim, S.. 2021. *Study on the effect of pore-scale heterogeneity and flow rate during repetitive two-phase fluid flow in microfluidic porous media. Petroleum Geoscience*, 27(2), pp.petgeo2020-062.